Fast Voltage Recovery Control of Wind Farm With Energy Storage Considering Coupling of Active Power and Voltage in Weak Grids

Qihang Zong, Wei Yao, *Senior Member, IEEE*, Hongyu Zhou, Jun Liang, *Fellow, IEEE*, Yongxin Xiong, *Member, IEEE*, Jinyu Wen, *Senior Member, IEEE*

***Abstract*—The weak grids containing wind power face a serious challenge: voltage recovery after faults is slow. Active power and voltage coupling (APVC) is one reason, but it has not yet been considered. Hence, this paper proposes a fast voltage recovery (FVR) control scheme for the wind farm with energy storage system (ESS). The coordination of the wind farm and ESS resolves APVC to obtain fast voltage recovery. Firstly, the APVC of the wind farm is quantitatively analyzed. As a key finding, the increase of active power output of wind farms during recovery has a negative coupling effect on voltage recovery. Moreover, the APVC is more significant in weak grids and low-voltage scenarios. Secondly, the FVR control based on preset curves is proposed, benefiting from the coupling analysis. In the early recovery stage with strong coupling, the ESS is coordinated to absorb active power. It transforms the negative effect of the coupling into a positive one to support voltage in priority. In the later recovery stage with weak coupling, the wind farm recovers active power with minimal effect on voltage. Finally, the results in two IEEE systems and real-time experimental platform verify the effectiveness of the proposed FVR control scheme.**

***Index Terms*—Wind farm, voltage recovery, active power and voltage coupling, energy storage, coordinated control**

I. Introduction

WIND power capacity continues to expand steadily in power systems worldwide [1], [2]. Meanwhile, the co-integration of the centralized energy storage system (ESS) with the wind farm has become commonplace [3]. Since 2021, the ESS allocation with 10% to 20% of the capacity of the wind farm is strongly recommended in China [4]. However, the voltage regulation capability of wind farms is significantly weaker than that of synchronous generators due to the power electronic converters for grid integration. Moreover, the near area of wind farms presents a low grid strength and the synchronous power supply is weak to support it [5]. As a result, the integration system with wind power faces severe voltage stability problems.

Manuscript received May 23, 2025; revised August 11, 2025; accepted September 12, 2025. This work was supported by National Natural Science Foundation of China (52537005, 523B2304). Paper no. TSTE-00693-2025 *(Corresponding author: Wei Yao)*.

Q. H. Zong, W. Yao, H. Y. Zhou, J. Y. Wen, are with State Key Laboratory of Advanced Electromagnetic Engineering and Technology, School of Electrical and Electronic Engineering, Huazhong University of Science and Technology, Wuhan 430074, China.(email: w.yao@hust.edu.cn).

Jun Liang is with the School of Engineering, Cardiff University, Cardiff CF24 3AA, U.K.

Yongxin Xiong is with Department of Electrical and Electronic Engineering, The Hong Kong Polytechnic University, 999077, Hong Kong, China

Fault-induced delayed voltage recovery is particularly prominent [6], [7], which is a critical type of short-term voltage stability problem. The voltage recovery problem is characterized by a slow recovery of the voltage from the low value to the normal level after the fault clearance, typically taking several seconds. Studies indicate that insufficient support from renewable energy stations exacerbates voltage stability issues and extends the voltage recovery time [8]. This will lead to off-grid operation as the wind farm voltage does not meet the ride-through requirements of grid codes. Furthermore, the slow voltage recovery can cause significant damage to power equipment and grid collapse. Consequently, enhancing the active voltage support capabilities of wind farms has become an urgent need.

To address this issue, current research primarily focuses on the reactive power regulation capability of wind turbine generators (WTGs) [9]. WTGs can release reactive power through flexible converters [10]. The voltage at the point of common coupling (PCC) of a wind farm is the main monitoring index and control target for station-level voltage regulation. The droop control of dynamic reactive current (DRC) is most commonly implemented in practical wind farm engineering. Specifically, WTGs inject reactive current that is linearly proportional to voltage deviation to support voltage. DRC has been explicitly mandated in the grid codes of several countries [11], [12]. Some studies further design Q–V droop control to enhance voltage support performance [13], as the control directly uses reactive power as the control increment. Ref. [14] builds upon the Q–V droop method by designing detailed data transmission and allocation schemes based on phasor measurement units. It improves the feasibility of voltage control applications. In addition, Refs. [15] and [16] propose adaptive Q–V droop methods utilizing data-driven. They aim to enhance closed-loop stability and coordination among multiple WTGs. The aforementioned methods are applicable throughout the entire low-voltage ride-through process and can improve voltage recovery dynamics to a certain extent. However, the reactive power capability of WTGs alone is often insufficient to meet the strong voltage support requirements in scenarios with deep voltage dips and power near limits [17].

As the other important type, coordinated voltage support controls involving auxiliary devices such as ESS alongside WTGs have been investigated. In [18], a voltage support logic for WTGs and ESS according to reactive power support requirements is studied. The core concept is utilizing the con-

verter of the ESS to supplement the reactive power when the reactive power capability of WTGs is insufficient. Moreover, Ref. [19] proposes an adaptive voltage control for combining WTGs and ESS (WEC control). The reactive power droop release of ESS is specially designed, in which ESS and WTGs are coordinated adaptively according to the severity of voltage sags. Similar to ESS, the reactive power coordination between WTGs and devices such as STATCOMs and SVGs has been explored for voltage support enhancement [12], [20], [21]. However, most of these coordination strategies simply regard ESS as an extension of the reactive power resources of WTGs [22], thereby failing to fully exploit the unique advantages of ESS. Consequently, the effectiveness of such coordination remains limited.

Notably, the above two types of methods generally use reactive power as the only object of analysis and control for voltage support. Nevertheless, the impact of active power dynamics on voltage recovery is largely overlooked. Only a few studies have attempted to account for this effect. Ref. [23] examines active power impacts on voltage under wind speed fluctuations in steady-state conditions. However, its impact is significantly different in the post-fault voltage recovery period. Because the voltage situation during recovery is worse. Moreover, the huge increase in the active power of WTGs from ride-through values to normal values needs to be realized within a short duration. Therefore, the impact of active power on voltage is a critical potential factor for voltage recovery but lacks analysis.

In this paper, a fast voltage recovery (FVR) control scheme for the wind farm is proposed, explicitly considering active power and voltage coupling (APVC). Specifically, the coupling characteristics are analytically derived and quantitatively analyzed to elucidate the impact of active power dynamics on voltage recovery. For better voltage recovery, a novel idea of utilizing active power regulation to support voltage is employed in the control. This scheme fully exploits the obtained characteristics of APVC. Furthermore, a complete coordinated control procedure is developed for WTGs and ESS. The main contributions of this paper are as follows.

- This paper proposes an FVR control of the wind farm with ESS considering the coupling of active power and voltage to support voltage recovery in weak grids. It transforms the coupling negative effect into a positive effect in the early recovery stage with strong coupling by coordinating the ESS to absorb active power. Subsequently, the active power of the wind farm is recovered during the later recovery stage with weak coupling. Therefore, this coordinated control significantly improves the voltage recovery performance compared to existing methods without considering APVC.
- APVC of the wind farm is quantitatively analyzed. Three important characteristics of APVC are further revealed. In conclusion, active power increase has a negative effect on voltage recovery, which is more significant in weak grid and low voltage scenarios. Furthermore, we discuss the comparison of the contribution to voltage by utilizing reversed APVC vs. conventional supply of reactive power. The superiority of absorbing active power to support voltage in weak grids is verified.
- A Logistic function-based reactive power release method for WTGs is designed to support voltage in addition to utilizing APVC. It leads to an inverse sigmoidal dependency between the voltage deviation and released reactive power. Compared with the linear and quadratic dependencies of traditional droop controls, this function enhances the reactive power release over a wide voltage deviation range to support voltage recovery. Moreover, the release allocation scheme among different WTGs is designed due to the wake effect.

The rest of the paper is organized as follows. The APVC during the recovery of the wind farm in weak grids is analyzed in Section II. Section III presents the proposed FVR control scheme for the wind farm with ESS considering the APVC. Case studies in two power systems are carried out in Section IV. Section V discusses the contribution of active and reactive power to voltage regulation. Section VI concludes the paper.

II. Active Power and Voltage Coupling Analysis of the Recovery of Wind Farms in Weak Grids

A. Slow Recovery of Wind Farm Voltage

Dynamic loads dominated by induction motors (IMs) are the core cause of fault-induced delayed voltage recovery. IMs account for about 40% of the load in the actual grid according to engineering research in western and northern provinces of China. Therefore, adequate consideration of IMs is necessary.

- During the fault duration period, the low voltage causes a reduction in electromagnetic power, the IM loses speed and the slip rate increases.
- After the fault clearance, the IM is at a low-speed condition in the early period. It has low power factor and absorbs large amount of reactive power. This period results in severe reactive power shortage in the system and delayed voltage recovery. In severe cases, this will lead to voltage instability of the continuous low voltage.

Slow voltage recovery is detrimental to loads and power electronics. As one of the results, slow voltage recovery leads to the PCC voltage of the wind farm triggering the safety boundary of the ride-through in grid codes. This threatens the safety of devices in the wind farm. And the forced off-grid of the wind farm will worsen the economics and stability of the system. This situation is becoming more obvious in weak grid scenarios. It further leads to a slower voltage recovery due to the weak ability of the grid side to provide reactive power.

B. Analysis of APVC of the Wind Farm

The wind farm enters recovery from ride-through mode after the fault clearance. It is necessary to recover the active power to the normal output value during the voltage recovery process. The role of APVC requires to be analyzed.

A long-distance transmission line links the wind farm to the grid, as shown in Fig. 1. Z_L is the impedance of the transmission line, which can also be expressed as $R_L + jX_L$. The short-circuit capacity $S_{\mathrm{ac,WF}}$ and the short-circuit ratio (SCR) can be calculated.

$$S_{\mathrm{ac,WF}} = \frac{E_g U_{\mathrm{PCC},N}}{X_L + X_g} \tag{1}$$

$$U_{\mathrm{PCC}}=\sqrt{\frac{2(\alpha P_{\mathrm{WF}}+Q_{\mathrm{WF}})\lambda+U_k^2\,\mathrm{SCR}+\sqrt{U_k^4\mathrm{SCR}^2+4(\alpha P_{\mathrm{WF}}+Q_{\mathrm{WF}})\lambda U_k^2\,\mathrm{SCR}+(8\alpha P_{\mathrm{WF}}Q_{\mathrm{WF}}-4P_{\mathrm{WF}}^2-4\alpha^2Q_{\mathrm{WF}}^2)\lambda^2}}{2\,\mathrm{SCR}}} \tag{5}$$

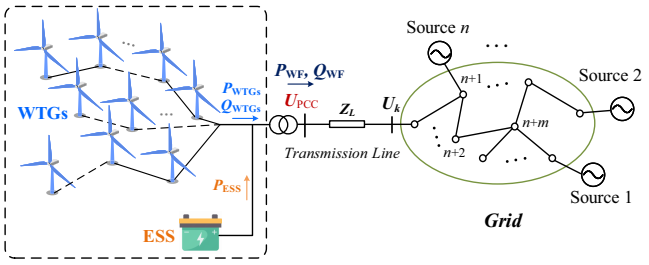

Fig. 1. Structure of wind farm connected to the power system with ESS.

$$\mathrm{SCR}=\frac{S_{\mathrm{ac,WF}}}{S_{g,\mathrm{WF}}}=\frac{1}{X_L+X_g}=\frac{\lambda}{X_L} \tag{2}$$

where $U_{\mathrm{PCC},N}$ is the rated voltage of the PCC. $S_{g,\mathrm{WF}}$ is the rated capacity of the wind farm. E_g and X_g are the electrical voltage and reactance of the grid-side equivalent by Davignan's theorem, respectively. λ is the ratio $X_L/(X_L+X_g)$, and satisfies $0<\lambda<1$.

The voltage at the wind farm PCC is established:

$$\dot{U}_{\mathrm{PCC}}=\dot{U}_k+\dot{I}_kZ_L \tag{3}$$

where $\dot{U}_k$ represents the voltage at the grid connection point of the transmission line. $\dot{I}_k$ is the current of the transmission line.

Refine the calculation of current and impedance in Eq. (3) to further obtain:

$$U_{\mathrm{PCC}}^*=\frac{U_{\mathrm{PCC}}^2-(P_{\mathrm{WF}}R_L+Q_{\mathrm{WF}}X_L)-j(P_{\mathrm{WF}}X_L-Q_{\mathrm{WF}}R_L)}{\dot{U}_k} \tag{4}$$

where U_{PCC}^* is the conjugate complex of the PCC voltage phasor. P_{WF} and Q_{WF} are the total active power and reactive power output from the wind farm to the main grid, respectively.

Combining Eqs. (1)-(4), a general expression for the PCC voltage is obtained as Eq. (5).

Define the APVC of the wind farm as ζ_{P-U}. It is a form of sensitivity that can be obtained by taking partial derivatives.

$$\begin{aligned}\zeta_{P-U}&=\frac{\partial U_{\mathrm{PCC}}}{\partial P_{\mathrm{WF}}}\\&=\frac{\lambda}{2U_{\mathrm{PCC}}\,\mathrm{SCR}}[\alpha+\frac{\alpha U_k^2\,\mathrm{SCR}+2\lambda(-P_{\mathrm{WF}}+Q_{\mathrm{WF}}\alpha)}{M_1}]\end{aligned} \tag{6}$$

$$\begin{aligned}M_1=&[\mathrm{SCR}^2\,U_k^4+4\,\mathrm{SCR}\,U_k^2\lambda(\alpha P_{\mathrm{WF}}+Q_{\mathrm{WF}})-4\lambda^2(P_{\mathrm{WF}}^2\\&-2P_{\mathrm{WF}}Q_{\mathrm{WF}}\alpha+Q_{\mathrm{WF}}^2\alpha^2)]^{\frac{1}{2}}\end{aligned} \tag{7}$$

where α is the ratio of resistance and inductance for the transmission line, which can be expressed as R_L/X_L.

For the wind power transmission system, the voltage level of the transmission line is above 110 kV. Therefore, the ratio α can be approximated as 0. The simplification is discussed in Section V. The coupling after simplified approximation ζ_{P-U}^s is expressed as:

$$\zeta_{P-U}^s=-\frac{\lambda^2P_{\mathrm{WF}}}{U_{\mathrm{PCC}}\,\mathrm{SCR}\,M_2} \tag{8}$$

$$M_2=\sqrt{\mathrm{SCR}^2\,U_k^4+4\,\mathrm{SCR}\,U_k^2\lambda Q_{\mathrm{WF}}-4\lambda^2P_{\mathrm{WF}}^2} \tag{9}$$

Eq. (8) establishes a quantitative relationship between APVC and three key parameters: the SCR, PCC voltage, and wind farm output power. Notably, the coupling is found to be negative ($\zeta_{P-U}^s<0$). This means that a marginal increase in the active power output of the wind farm will cause a drop in the PCC voltage. Thus, APVC is a contribution of active power to voltage, which is further discussed in Section V.

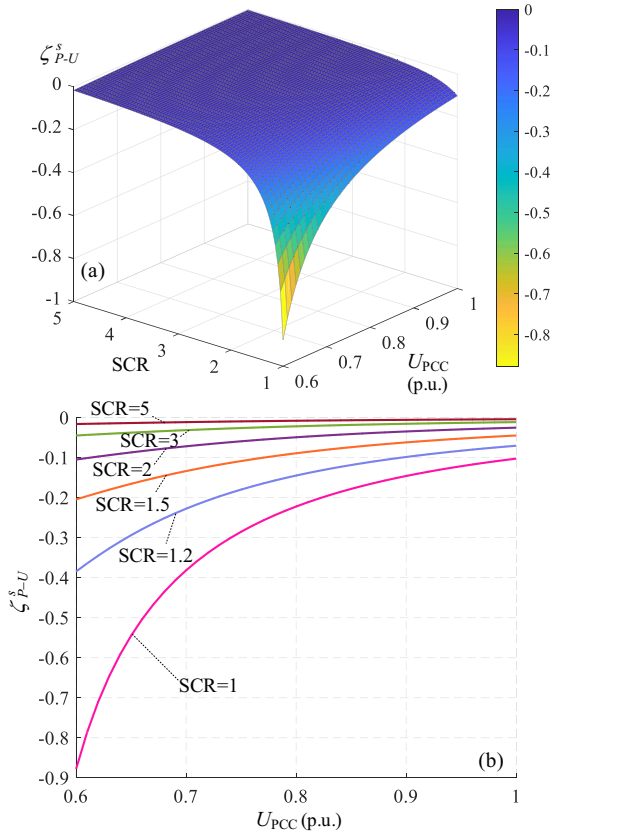

Fig. 2. Coupling of active power-voltage for wind farms with different SCR and U_{PCC}. (a) 3D view. (b) Side view.

Conclusively, several characteristics are obtained by Eq. (8):

1) Characteristic I: The increase of active power output of the wind farm during recovery has a negative effect on voltage recovery. The larger absolute value of the coupling $|\zeta_{P-U}^s|$ implies a more severe voltage worsening effect caused by the increase of active power.

2) Characteristic II: The weaker the grid strength SCR, the more severe the APVC. Especially, the negative effect of APVC is significant in very weak grids with SCR < 2.

3) Characteristic III: The lower voltage at the point of common coupling U_{PCC}, the more severe the APVC.

The coupling with varying SCR and U_{PCC} under typical parameters is shown in Fig. 2, which clearly verifies the above characteristics.

C. APVC for Voltage Recovery Period

The above characteristics I and II are easy to comprehend, which corroborates the specificity of the voltage recovery problem faced in weak grids. Hence, the time-series properties of the voltage recovery process are elaborated with characteristic III. To elaborate more clearly, the APVC analysis using phasor diagrams is shown in Fig. 3.

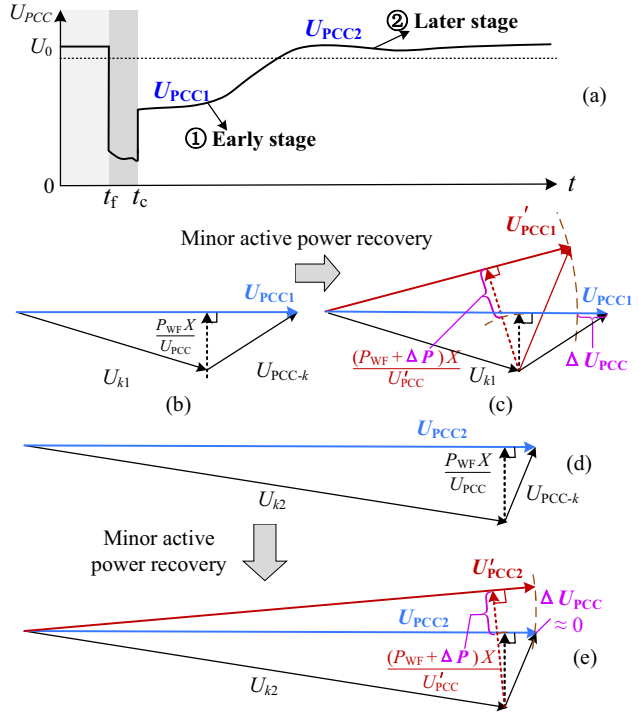

Fig. 3. APVC analysis during voltage recovery process using phasor diagrams. (a) PCC voltage dynamics. (b) Original phasor diagram in the early recovery stage. (c) Phasor diagram with a minor active power increase in the early recovery stage. (d) Original phasor diagram in the later recovery stage. (e) Phasor diagram with a minor active power increase in the later recovery stage.

1) Early recovery stage: This stage is from the fault clearance until the PCC voltage returns to the normal range for the first time. During the early recovery stage, the voltage level U_{PCC} is low while the APVC is strong. It will cause a large voltage drop if the wind farm increases a minor active power ΔP (i.e., active power recovery), as shown in the comparison of Fig.3 (b) and (c). Although voltage has a tendency to recover with the gradual lack of system reactive power shortage, active power recovery will significantly delay voltage recovery. The weak grid is prone to voltage drop and breakdown during the recovery process.

2) Later recovery stage: This stage is from the time PCC voltage returns to the normal range until the voltage levels off to a steady-state value. During the later recovery stage, the voltage level U_{PCC} is high while APVC is weak. The effect of increasing the same active power ΔP by the wind farm on the voltage magnitude is weak, as shown in the comparison of Fig. 3 (d) and (e). This is due to the fact that the voltage phase change by the increase in active power is much smaller in this case compared to the previous case.

In summary, the negative effect of APVC is strong in the early stage of voltage recovery. By contrast, the negative effect of coupling is weak in the later stage of voltage recovery.

III. Proposed FVR Control for WTGs with ESS Considering Active Power and Voltage Coupling

A. Core Idea on Active power and voltage Coupling

As discussed in Section II, there is strong APVC in the weak grid during the early recovery stage. But conventional voltage controls rapidly increase the active power in this period. It leads to voltage worsening. Table I compares the differences in characteristics between these two recovery stages.

TABLE I
Comparison of the Characteristics of the Early and Later Recovery Stages

Stages of recovery	Differences in typical characteristics			Difference of core concern
	Voltage level	Degree of coupling	Impact of active power recovery	Impact of active power absorption
Early stage	Low	Strong	Large voltage drop (Negative)	**Large voltage rise (Positive)**
Later stage	High	Weak	**Minor voltage drop (Negative)**	Minor voltage rise (Positive)

Benefiting from the obtained characteristics, the core idea of the proposed FVR control scheme for the APVC problem is shown as follows and in Fig. 4.

- *Early stage of recovery with strong coupling:* Utilizing the centralized ESS within the wind farm to absorb active power. As shown in the last column of Table I, such a reverse active power shift transforms the coupling negative effect of characteristic I into a positive effect. Its purpose is to support the voltage preferentially.
$$\zeta^{ab}_{P-U} = -\zeta^{s}_{P-U} > 0 \tag{10}$$
where ζ^{ab}_{P-U} is the APVC of the wind farm in terms of absorbing active power.
- *Later stage of recovery with weak coupling:* The wind farm increases the active power. WTGs recover active power but have only a minor negative effect on voltage.

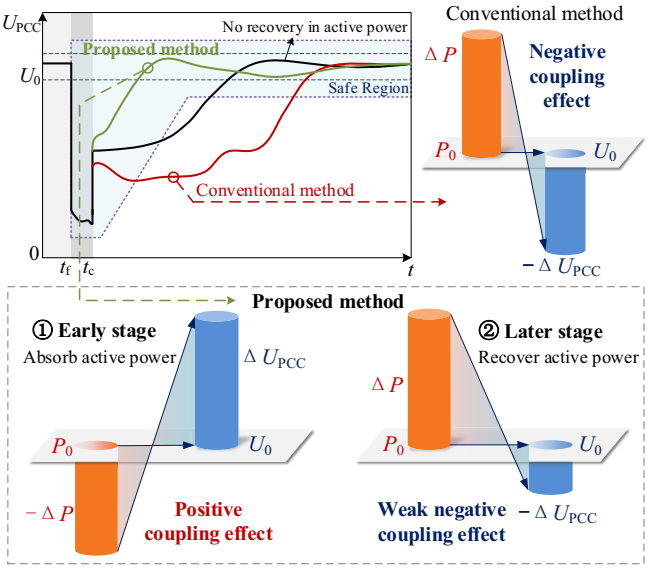

Fig. 4. The core idea of the proposed FVR control on the effect of APVC.

The particularity of absorbing active power rather than releasing reactive power by ESS in the early stage is discussed in Section V. Besides faster voltage recovery, the energy stored in the ESS can reduce wind energy abandonment.

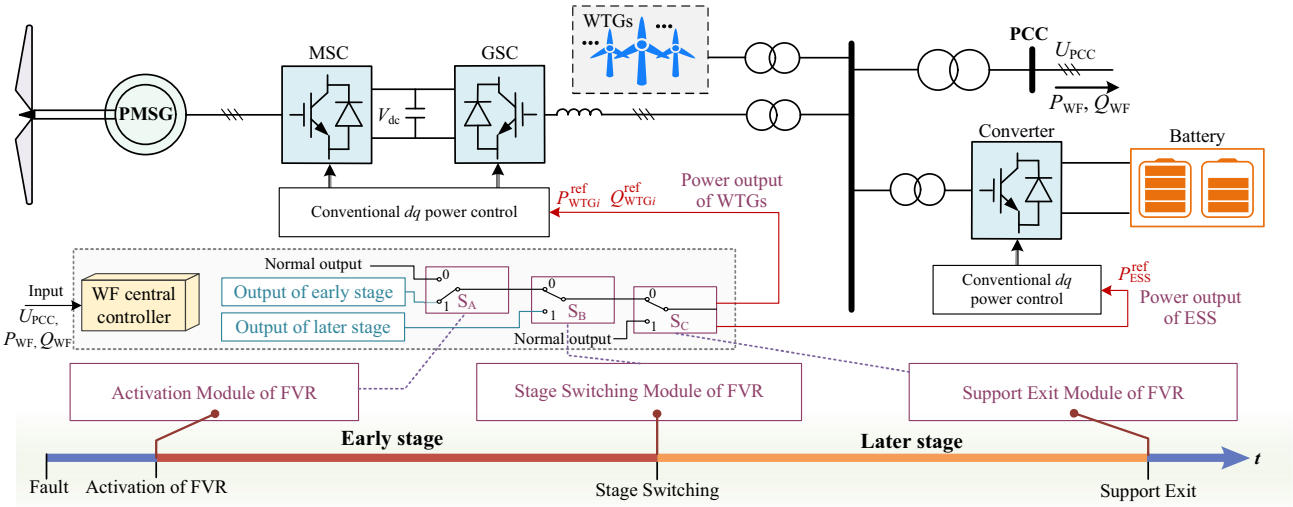

Fig. 5. Framework and timing actions of the proposed FVR control of WTGs coordinated with ESS.

B. Specific Modules of FVR Control for the Wind farm

The proposed FVR control is presented in Fig. 5. The logic modules for activation, switching, and exit of the support are undertaken by the central controller of the wind farm. Moreover, it sends power reference values to the WTGs and ESS. The converters of the WTGs and ESS adopt the traditional double closed-loop control structures and do not require modification.

1) Activation module of FVR: The voltage recovery control is required to be activated quickly after fault clearance. The activation module monitors the PCC voltage U_{PCC}. The activation criterion for FVR is defined as: U_{PCC} is below the voltage threshold U_{low} and the surge value ΔU_{PCC} is greater than the threshold value ΔU_c within 10 ms. According to IEEE Std 1547a-2020 and GB/T 19963.1-2021, U_{low} and ΔU_c are selected as 0.9 p.u and 0.1 p.u., respectively. 10 ms is the sampling interval of phasor measurement units (PMUs) used. When the activation criterion is satisfied, the logic switch S_A is set to 1 and FVR control is enabled. It is intended to utilize the local data of the PCC to obtain the status of fault clearance. As a result, it reduces the communication requirements and shortens the start-up time.

2) Stage switching module of FVR: With the voltage gradually recovering due to the support, the absolute value of APVC decreases. The requirements for switching are low coupling and high voltage values. The specific switching criterion is that the absolute value $|\zeta^s_{P-U}|$ of the wind farm is less than the coupling threshold ζ_{low} (0.1p.u.) as well as the voltage U_{PCC} is greater than the voltage threshold U_1 (0.97p.u.) within a continuous period of 300ms. The values of the threshold and time window are based on GB/T 19963.1-2021 and the grid code from E.ON.

The APVC is monitored in real time ζ^s_{P-U} by Eqs. (8)-(9) and (11). Specifically, X_L is required as a known parameter. For the real-time measurement, P_{WF}, Q_{WF}, and U_{PCC} are easily measured via the PMU. From Eq. (2), SCR is available if X_L+X_g is obtained in real-time. According to the impedance identification algorithm [24], [25], the required reactance of X_L+X_g can be obtained by injecting a harmonic voltage and detecting the response harmonic current. Since both the numerator and denominator of $X_L/(X_L$+$X_g)$ have been obtained, λ can be further calculated.

$$U_k^2 = (U_{\mathrm{PCC}} - \frac{Q_{\mathrm{WF}} X_L}{U_{\mathrm{PCC}}})^2 + \frac{P_{\mathrm{WF}}^2 X_L^2}{U_{\mathrm{PCC}}^2} \tag{11}$$

3) Support exit module of FVR: When the recovery of the active power and voltage of the wind farm is completed, the support control shall smoothly exit and transition to the normal state. The recovery completion condition is recognized by monitoring the voltage. The designed voltage recovery completion criteria is: the voltage U_{PCC} is neither lower than U_1 (0.97p.u.) nor higher than U_2 (1.07p.u.) within 2s. This time window is appropriately extended compared to the Tennet TSO requirements. The criterion requires that the PCC voltage has not only recovered to the normal range, but has gradually leveled off to the steady state. Such a design contributes to the smoothness of the exit.

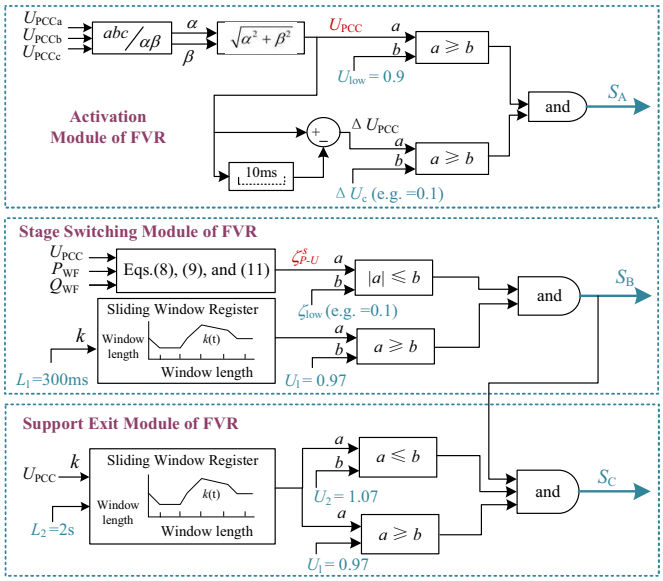

Fig. 6. Specific modules for the proposed FVR control.

4) Power output of WTGs: The power output of the WTGs follows the preset curves elaborated in subsection III-C. In particular, the reactive power output is specially designed. As presented in Fig. 7, the voltage supports of conventional grid code and typical Q-V droop are able to adaptively provide reactive power output according to the voltage deviation. However, they behave as quadratic and linear functions in reactive power characteristics, respectively. This leads to insufficient

utilization of reactive power resources at non-maximum deviations, especially in the deadband range of voltage deviation of ±0.1p.u.. In contrast, the designed reactive power output of the whole WTGs is modeled as a Logistic function. This Q-Logistic method has the advantage of smoothly and optimally releasing reactive power over a wide voltage deviation range. Hence, it further supports the voltage recovery faster.

$$Q^*_{\mathrm{WF}} = \frac{K_0[e^{\alpha(U_{\mathrm{PCC}}-U_{\mathrm{ref}})}-1]}{e^{\alpha(U_{\mathrm{PCC}}-U_{\mathrm{ref}})}+1} \tag{12}$$

where, K_0, α are the boundary and droop coefficients, respectively. U_{ref} is the reference of PCC voltage. Q^*_{WF} is the reactive power expected to be released by the wind farm.

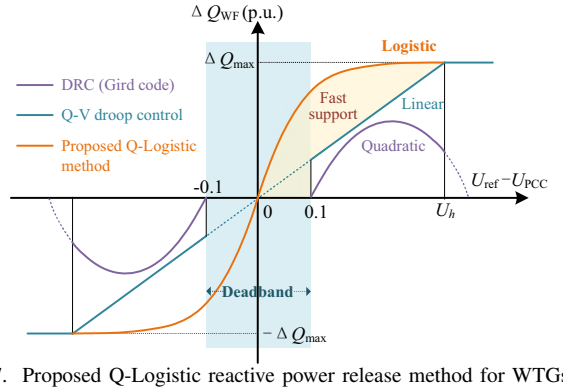

Fig. 7. Proposed Q-Logistic reactive power release method for WTGs.

The wake effect causes the real-time power of each WTG to be different. It results in different available capacities of WTGs to support the voltage. An average distribution of reactive power release will cause some of the units with low available capacities to exceed their power limits. To fully utilize the available capacities of WTGs, the power distribution among multiple WTGs is coordinated in the proposed FVR control, as illustrated in Fig. 8. Specifically, the green bar is the real-time available capacity of each WTG for support. And the available capacity ratio γ_i is calculated for each WTG.

$$\gamma_i = \frac{S_{\max} - \sqrt{P^2_{\mathrm{WTG}i} + Q^2_{\mathrm{WTG}i}}}{S_{\max} - S_{\min}} \tag{13}$$

where $S_{\max}$ and $S_{\min}$ are the maximum and minimum capacities of each WTG, respectively. $P_{\mathrm{WTG}i}$ and $Q_{\mathrm{WTG}i}$ are the active and reactive powers of the i-th WTG.

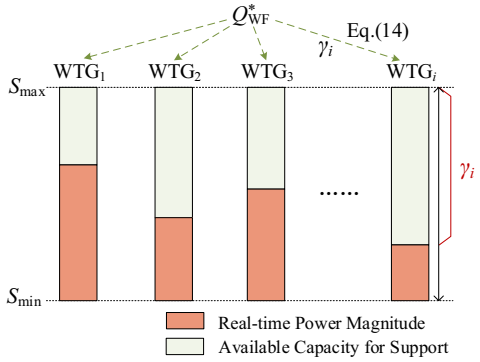

Fig. 8. Coordinated distribution of reactive power release among WTGs.

Further, the expected reactive power of the Q-logistic method in Eq. (12) is distributed among the multiple WTGs according to the available capacity ratios, as shown in Fig.8. Its advantage is to ensure the exhaustive utilization of the different WTG capacities under safety requirements.

$$Q_{\mathrm{WTG}i,\mathrm{ref}} = \frac{\gamma_i}{\sum_{i=1}^{N}\gamma_i} Q^*_{\mathrm{WF}} \tag{14}$$

where $Q_{\mathrm{WTG}i,\mathrm{ref}}$ is the reactive power reference of the i-th WTG. N is the total number of WTGs.

5) Power output of centralized ESS: The designed FVR control mainly focuses on the coordination of the active power of the ESS. The active power output of the ESS also follows the preset curve in subsection III-C. Active power is absorbed and released according to the slope k_{ESS}.

C. Complete FVR Control Scheme Based on Preset Curves

The preset curves of active power and reactive power of the WTGs and ESS are shown in Fig. 9, respectively. 0∼t_f is the normal operation period, t_f∼t_c is the fault duration period, and t_c is the fault clearing moment. For clearer presentation, the flowchart of the proposed FVR control is illustrated in Fig. 10. The detailed FVR support process is further elaborated.

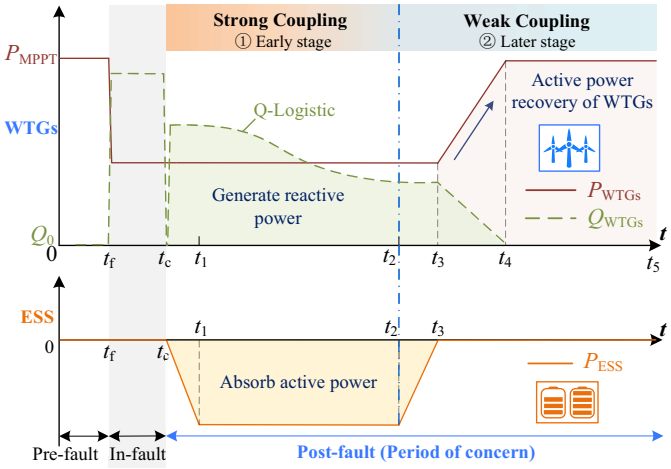

Fig. 9. Designed active power and reactive power output of WTGs and ESS based on preset curves.

1) Early stage of recovery: Due to the strong APVC in the early recovery period, the ESS provides support to the voltage by absorbing active power during this period. The yellow area in Fig. 9 represents the stored energy from active power absorption by the ESS. Meanwhile, the WTGs provide reactive power rapidly by the proposed Q-Logistic release method, as shown by the green line.

- *Early recovery stage I (t_c∼t_1):* The activation module of FVR monitors the satisfaction of the activation criterion (S_A=1) soon after t_c, and the FVR control is activated. The startup takes about 10∼20 ms. The support enters the early stage of recovery. The WTGs employ the reactive power control of the Q-Logistic function to increase reactive power, and the active power remains at the ride-through value. Meanwhile, ESS absorbs the active power by climbing gradually with the slope k_{ESS}.
- *Early recovery stage II (t_1∼t_2):* As the ESS increases the active power absorption continuously, the active power value reaches the maximum value at t_1. Thereafter, the ESS maintains the maximum power value for continuous

active power absorption. At the same time, the WTGs continue to release reactive power as above.

2) Later stage of recovery: Due to the weak APVC in the later recovery period, WTGs perform active power recovery (red region). The ESS exits the active power absorption state.

- *Later recovery stage I (t_2∼t_3):* When the FVR stage switching module recognizes that the switching criterion is satisfied (S_B=1), the switching FVR control enters the later stage of recovery. The switching moment is t_2, and the switching action takes 10 ms. Currently, the ESS gradually reduces the absorbed active power in accordance with the slope k_{ESS} until 0.
- *Later recovery stage II (t_3∼t_4):* Since the ESS completely exits the active power absorption state (t_3), the active powers of the WTGs start to recover to the normal value by the slope. And the reactive powers decrease to normal values gradually in a similar manner.
- *Later recovery stage III (t_4∼t_5):* The active power of each WTG is raised to the MPPT value at t_4. Thereafter, the WTGs maintain normal active and reactive power output. Moreover, the ESS maintains the power output at 0. It ensures that the power values are equal to those of the normal state, further contributing to the smooth exit.
- *FVR control exit (t_5):* The wind farm officially exits the voltage recovery state and enters the normal operation state when the exit module is activated (S_C=1).

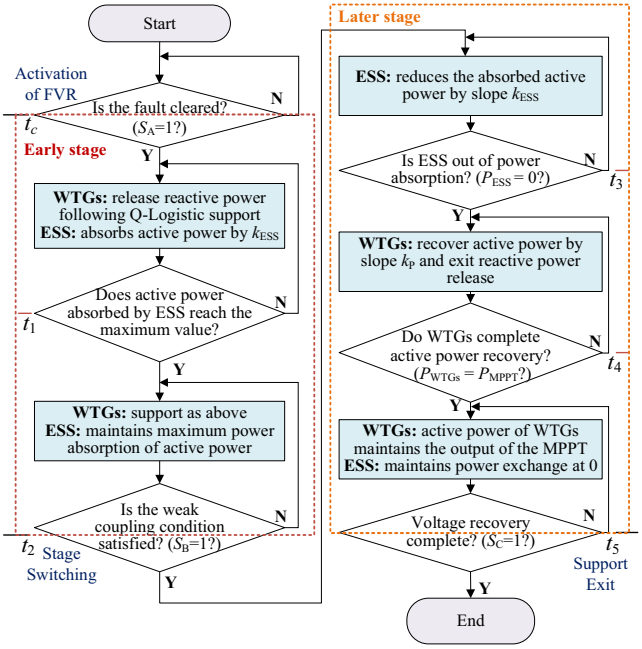

Fig. 10. Flowchart of the actual application of the proposed FVR control.

IV. Case Studies

The IEEE two-area system with a wind farm is established on the MATLAB/Simulink using the MatPSST toolbox [27], as presented in Fig. 11. For the WTGs, the type-4 model of WTG from the International Electrotechnical Commission (IEC) is used for simulation [28]. This model is composed of a permanent magnet synchronous generator and full-scale back-to-back power electronic converters. The wind farm consists of 15 equivalent WTGs. Each equivalent WTG is aggregated from 10 turbines with a rated capacity of 3.33 MW. The capacity penetration of wind power is 24.3%. The parameters of the wind farm are from the project located in the Bazhou region of southern Xinjiang province, China. For the ESS, the model consists of two components: the module of the battery device and the power conversion system. To account for battery polarity and avoid complexity, the typical first-order Thevenin model of the battery is employed. The ESS capacity is 10% of the total capacity of the WTGs, equating to 50MW. For the power system, the model of Fig. 11 replaces one synchronous generator in the standard two-area system of Kundur [29] with a wind farm. The real power of the other generators is 555 MW, 600 MW, and 650 MW. The base capacity is 100 MVA, and the rated frequency is 50 Hz. On no particular note, the SCR is 1.2 and the IM load share is 40%. The third-order model of IM is used as [30]. Other parameters are available in the Appendix. Table II lists the control schemes compared in this section.

The simulation horizon is set to 9 s. This is because the fault and recovery period is typically within 5 s. The setting clearly simulates the complete process. The variable-step solver ode15s is configured with a maximum time step of 0.1s and a minimum step of 10^{-6}s, ensuring both computational efficiency during steady states and accuracy during recovery.

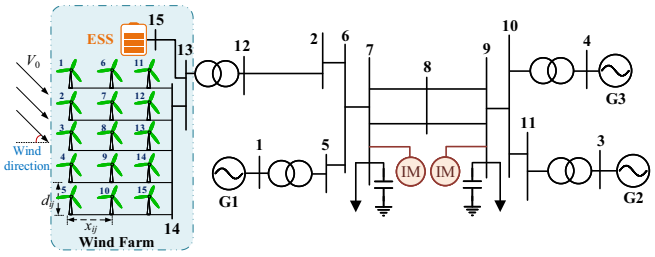

Fig. 11. Structure of the IEEE two-area integration system with a wind farm.

A. Verification of Active Power and Voltage Coupling

To validate the characteristics analysis of the wind farm APVC in Section II, two cases in the weak and strong grids are carried out separately. A three-phase-to-ground fault occurs at

TABLE II
Descriptions of Different Control Schemes

Control		Description	WTGs support (Q)	Active power recovery	ESS support
Comparative	DRC	Dynamic reactive current control [26]	✓	✓	×
	DRC-R	Dynamic reactive current control without active power recovery	✓	×	×
	Q-V droop	Reactive power-voltage droop control	✓	✓	×
	WEC	Coordinated control of wind turbines and energy storage [19]	✓	✓	✓ (Q)
Proposed	FVR	Proposed fast voltage recovery control	✓	✓	✓ (P)

** (P) means the control object is active power. * (Q) means the control object is reactive power.*

t_f = 5.0s. It is located 20% near bus 8 in line 7-8. It is cleared at t_c = 5.25s. The voltage recovery time t_{rec} is from t_f until the U_{PCC} is recovered to the voltage normal range (0.97 $\sim$ 1.07 p.u.). Refer to Fig. 12 for the detailed results. DRC-R control is the DRC control without active power recovery, as shown in Table II and Fig. 12(b). It is used as a comparison with the conventional DRC control to validate the APVC.

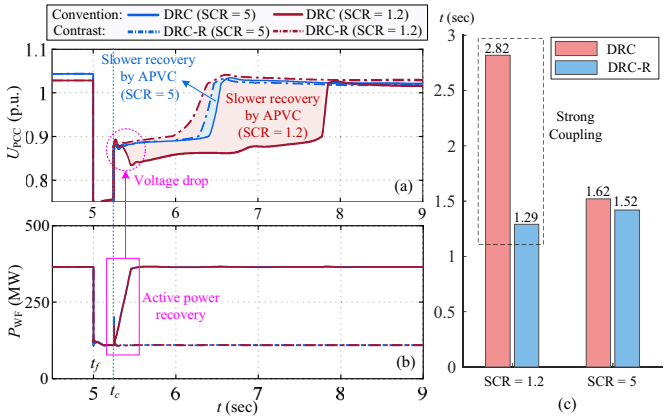

Fig. 12. Voltage recovery results in very weak grid (SCR = 1.2) and strong grid (SCR = 5.0). (a) PCC voltage. (b) Active power of WTGs. (c) Comparison of recovery time.

1) Weak grid case with SCR = 1.2: The voltage using conventional DRC control shows slow recovery dynamics. Moreover, the rapid recovery of the active power in the early period leads to a sharp voltage drop. The voltage returns to normal range at t = 7.82s with t_{rec} of 2.82s. By contrast, the t_{rec} is much shorter as 1.29s using DRC-R control. The significant difference between the two is due to the negative effect caused by APVC, as shown by the red area in Fig. 12(a). Therefore, this verifies the characteristic I of APVC, i.e., the negative effect of active power increase on voltage recovery.

2) Strong grid case with SCR = 5.0: The voltage recovery time using conventional DRC control is 1.62s. While it is 1.52s with DRC-R control. There is little difference between the two, as shown by the blue area in Fig. 12(a).

The comparison of the above cases and Fig. 12(c) validate the characteristic II of APVC, i.e., APVC is significant and cannot be ignored in the weak grids.

B. Performance of Proposed FVR Control under Weak Grids

To illustrate the proposed FVR control and advantages in detail, a case of weak grid SCR = 1.2 is analyzed in this section. Specifically, the same fault occurs at t_f = 5s near bus 7 on line 7-8. It lasts for 0.21s. The recovery results are shown in Fig. 13.

1) Implementation of FVR control and comparison: Several controls are carried out for comparison. For the DRC control [26], the PCC voltage is recovered at t = 7.51s with the recovery time of t_{DRC} = 2.51s. And the voltage stays below 0.9 p.u. until t = 7.0s, as shown in Fig. 13(a). This does not satisfy the grid code and will result in the WTGs being off-grid. For the Q-V droop control of WTGs, the voltage recovery time is reduced to 2.11s owing to better reactive power release. And the voltage satisfies the grid code. However, their voltage recoveries are all slow. For the WEC control of WTGs coordinated with ESS [19], the voltage recovery dynamics are enhanced. This is because the ESS is coordinated to release the reactive power maximally, which is illustrated in Fig. 13(b). The voltage recovery time is then reduced to t_{WEC} = 1.86s.

The logical switches and stages of FVR control are shown in Fig. 13(f).

- *Early recovery stage.* The FVR control is activated at t = 5.22s due to the activation module with S_A = 1. The support enters the early recovery stage. And the ESS starts to absorb active power as shown in Fig. 13(d). It absorbs to the maximum power limit at t_1 = 5.42s. Meanwhile, the WTGs rapidly release reactive power after activation by the proposed Q-Logistic method. The total reactive power is presented in Fig. 13(c). From Fig. 13(a), the voltage is raised fast in the early stage. It is because the inversely utilizing APVC and enhanced reactive power release both better support the voltage.
- *Later recovery stage.* Due to voltage and coupling satisfying the stage switching module requirement (S_B = 1) at t_2 = 6.35s, the control enters the later recovery stage. The ESS gradually exits the active power absorption state. It has completely exited power absorption at t_3 = 6.55s. And the WTGs reduce reactive power response and recover

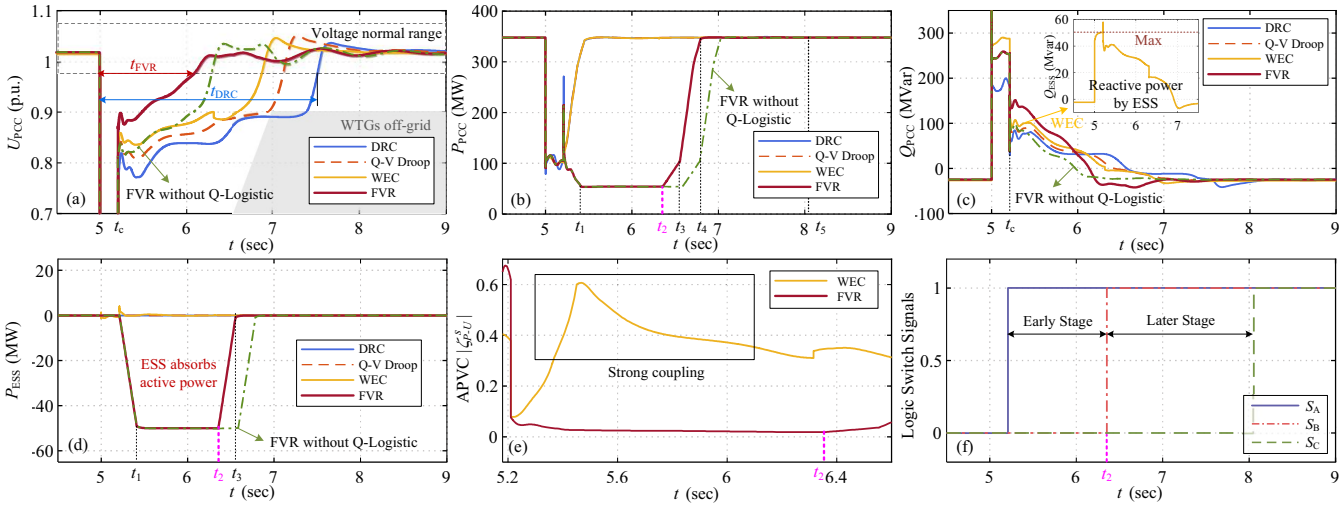

Fig. 13. Results of voltage recovery for the wind farm in a weak grid with SCR = 1.2. (a) PCC voltage. (b) Total active power of PCC. (c) Total reactive power of PCC. (d) Active power of ESS. (e) Real-time APVC. (f) Logic switches of the FVR control.

active power after t_3. Their active powers have recovered completely at t_4 = 6.80s. Finally, the FVR control exits at t_5 = 8.05s due to the support exit module with S_C = 1.

In summary, the voltage recovery time t_{FVR} using FVR control is 1.05 s. It is 43.5% improved compared to the coordinated control of WEC, which also utilizes the ESS capacity. Compared to DRC and Q-V droop control, the improvement is more than 50%.

2) Role of active power regulation: To illustrate the advantage of supporting voltage by active power in this paper more clearly, a comparative control that removes the enhanced reactive power release is shown. The results are presented as green dashed lines in Fig. 13. This control retains the active power coordination design. However, the WTGs only use the Q-V droop control. Fig. 13(c) demonstrates that this comparative control releases less reactive power than any control. However, it has a better voltage support effect than other controls with a recovery time of 1.28s. It verifies the main role of utilizing active power to support the voltage recovery as proposed.

3) Coordination among multiple WTGs: As shown in Fig. 11, the wind direction is the angle between the wind and the row direction of the WTGs. In the case of this paper, the wind direction is selected as 45°. The wind speed is set to 16.0 m/s. The wake effect between multiple WTGs is calculated by the Jensen's model as in the Appendix. Wind speed of each WTG considering wake effects: [16.00, 16.00, 16.00, 16.00, 16.00; 16.00, 13.95, 13.95, 13.95, 13.95; 16.00, 13.95, 13.70, 13.70, 13.70]. The power states of the WTGs are not the same due to the wake effect. Fig. 14 shows the specific reactive and active power outputs of each unit using FVR control in the early recovery stage (e.g., t = 5.30s) and the later recovery stage (e.g., t = 6.60s), respectively. This is because the power allocation takes into account the unit states in Eq. (14). Therefore, the effectiveness of coordination among WTGs is verified.

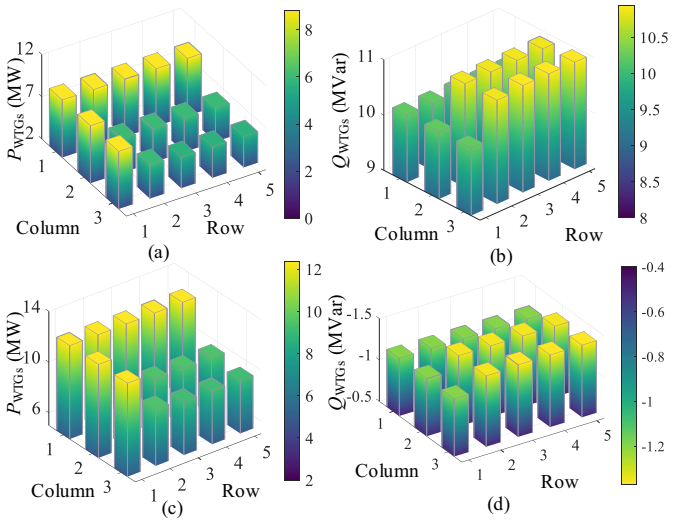

Fig. 14. Active and reactive powers of WTGs in the wind farm of the weak grid case. (a) Active powers at t = 5.30s. (b) Reactive powers at t = 5.30s. (c) Active powers at t = 6.60s. (d) Reactive powers at t = 6.60s.

C. Support Effects under Different Dynamic Load Ratios

Since different proportions of IM affect the voltage recovery dynamics, The tests on the adaptability of the FVR control to IM ratios are carried out. The IM load ratios in the above system are set to 20%, 30%, 40%, and 50%, respectively. That covers most of the actual engineering scenarios. The fault and SCR settings are the same as in subsection IV-B. Fig. 15 shows the voltage recovery results at different IM ratios.

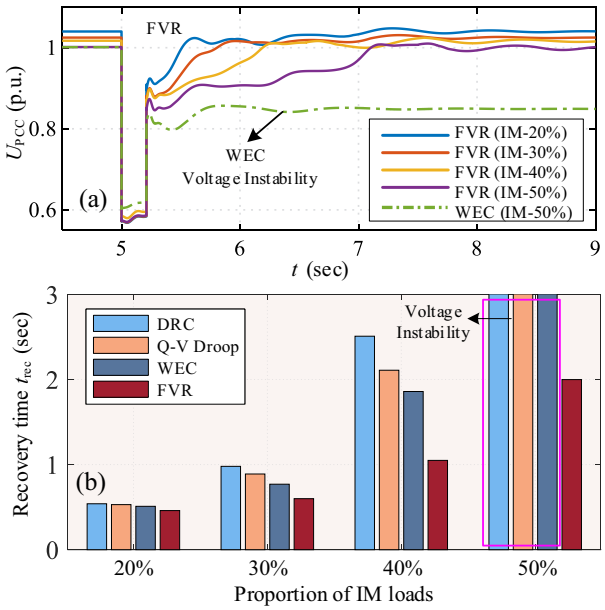

Fig. 15. Voltage recovery results at different IM ratios. (a) PCC voltage recovery dynamics. (b) Voltage recovery time.

From Fig. 15(a), the FVR control supports voltage recovery at different ratios. Although the voltage recovery is slower as the IM ratio increases. This is due to the more reactive power absorbed by the IM load during recovery. However, other controls such as WEC control are not sufficient to support voltage recovery at an IM ratio of 50%. It leads to voltage instability. Fig. 15(b) shows the voltage recovery time for different IM ratios. The recovery time is improved by at least 9.8%, 22.1%, and 43.6% using FVR control at 20%,30%, and 40% ratios, respectively. In particular, only FVR control supports fast voltage recovery at the 50% ratio with a recovery time of 1.99s.

D. Support Effects under Different Fault Conditions

To further validate the FVR control under different fault scenarios, the fault duration is set to 100ms, 200ms, 300ms, and 400ms, respectively. The fault type and SCR settings are the same as described above. And the IM ratio is set to 30% for comparison directly. Table III shows the voltage recovery performance in these conditions.

From the results, the FVR control has superior voltage support performance in different cases. Using the FVR control, the average voltage U_{avg} and the minimum voltage U_{min} during recovery are improved by 0.06 p.u. and 0.065 p.u., respectively. Besides, the recovery time is improved by 26.9% on average. In particular, only the FVR control enables the voltage to satisfy the grid code at a fault duration of 400ms. This demonstrates its excellent adaptability to harsh conditions.

TABLE III
VOLTAGE RECOVERY PERFORMANCE UNDER DIFFERENT CONDITIONS

Fault Duration (sec)	Control methods	Dynamic characteristics			Satisfaction of grid code
		U_{avg} (p.u.)	U_{min} (p.u.)	t_{rec} (sec)	
0.1	DRC	0.88	0.79	0.38	Satisfy
	WEC	0.89	0.83	0.37	Satisfy
	FVR	**0.94**	**0.89**	**0.29**	**Satisfy**
0.2	DRC	0.85	0.80	0.78	Satisfy
	WEC	0.86	0.83	0.76	Satisfy
	FVR	**0.93**	**0.89**	**0.59**	**Satisfy**
0.3	DRC	0.86	0.78	1.76	Satisfy
	WEC	0.87	0.82	1.65	Satisfy
	FVR	**0.93**	**0.88**	**1.18**	**Satisfy**
0.4	DRC	0.85	0.69	3.86	Failure
	WEC	0.86	0.77	3.37	Failure
	FVR	**0.92**	**0.85**	**2.19**	**Satisfy**

* U_{avg} *is the average voltage from* t_c *to voltage recovery.*
* U_{min} *is the minimum voltage from* t_c *to voltage recovery.*

E. Effect of Time Latency

To verify the effectiveness of the proposed control with time latency, a total latency of 55ms is set. According to IEC 61400-25 [31], the following specific latencies are considered: (a) 40ms of communication delay is set, according to [32], [33]. This delay is the main latency and contains the data and command exchange between the central controller and the turbine controller. (b) 4ms of data encoding and decoding time by controllers. (c) 10ms of sampling time for the monitoring data. (d) 1ms of computation time for the central controller. The results under time latency to the voltage event (in Fig. 13) are shown in Fig. 16. From the results, the proposed FVR control still enables fast voltage recovery. As shown in Fig. 16(a), due to latency, the reactive power references of WTGs remain at significantly elevated levels corresponding to the fault period for tens of milliseconds after t_c. This leads to a brief voltage increase and even promotes a reduction of the total recovery time. With time latency, the recovery time with FVR control is 1.02s, which is a 40.4% improvement compared to the WEC control. From Fig. 16 (d) and the enlarged subfigures in (a), (b), (c), the stage transitions are smooth and stable even with a latency of 55ms. The delayed arrival of control commands does not cause the controller state to be disordered.

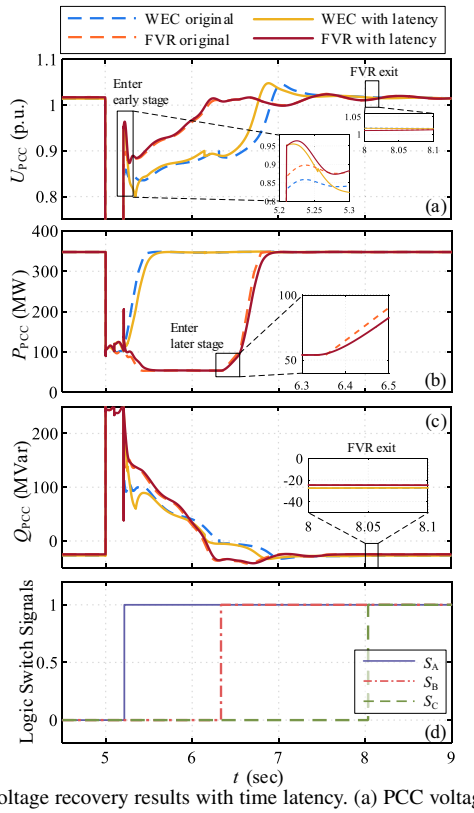

Fig. 16. Voltage recovery results with time latency. (a) PCC voltage. (b) Total active power of PCC. (c) Total reactive power of PCC. (d) Logic switches.

F. Verification in New England 39-bus System with Wind Farms

To evaluate the efficacy of the FVR control in a large-scale system, the New England 39-bus system with wind power is tested. Specifically, four wind farms replace the original synchronous generators G2, G3, G4, and G6. Every wind farm comprises five WTGs, each with a capacity of 100 MW. The system structure is described in [10]. In addition, the PCC of each farm is equipped with 10% ESS.

Ten cases are conducted for fault durations of 150ms, 200ms, 250ms, 300ms, and 350ms at bus 15 and bus 21 respectively. The SCRs of wind farms 3 and 4 are set to 1.4 and 1.3, respectively. Fig. 17 shows the results with the FVR control. The maximum voltage recovery time for the wind farm 3 is 1.30s. Further, it has an average recovery time of 0.82s. This is an enhancement compared to 1.11s for the DRC control. For wind farm 4, the average voltage recovery time is 0.65s. A 29.3% improvement is obtained. The applicability of the FVR control to large-scale systems is validated.

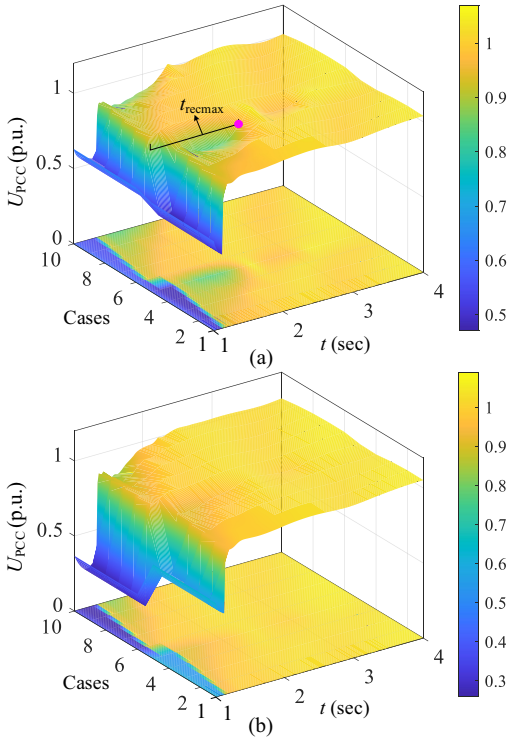

Fig. 17. Voltage recovery results of 10 cases in New England 39-bus system. (a) PCC voltage (wind farm 3). (b) PCC voltage (wind farm 4).

G. Real-time Experimental Verification

To experimentally validate the effectiveness, an Opal-RT real-time simulation platform is developed [34], [35]. It contains an OP4510 simulator and an OP5700 simulator, as shown in Fig. 18(a). The system in Fig.11 is established in the OP5700 simulator. While the OP4510 simulator is used to achieve the FVR control. The employed OP4510 features an Intel® Xeon® E3 multi-core high-performance CPU processor and a Xilinx® Kintex® 7 FPGA. A fixed time step of 10 μs is set. This significantly improves the actual physical validation condition of the controller with the FVR control. The OP4510 and OP5700 are interfaced through a conversion board with DB37 signal lines. As the experiment runs, OP4510 receives the PCC voltage signal sent by OP5700. In turn, OP4510 outputs the power reference values of WTGs and ESS (including $P^{\text{ref}}_{\text{WTG}i}$, $Q^{\text{ref}}_{\text{WTG}i}$, $P^{\text{ref}}_{\text{ESS}}$) to OP5700. These signals are affected by noise, quantization errors, transmission delays, and other factors.

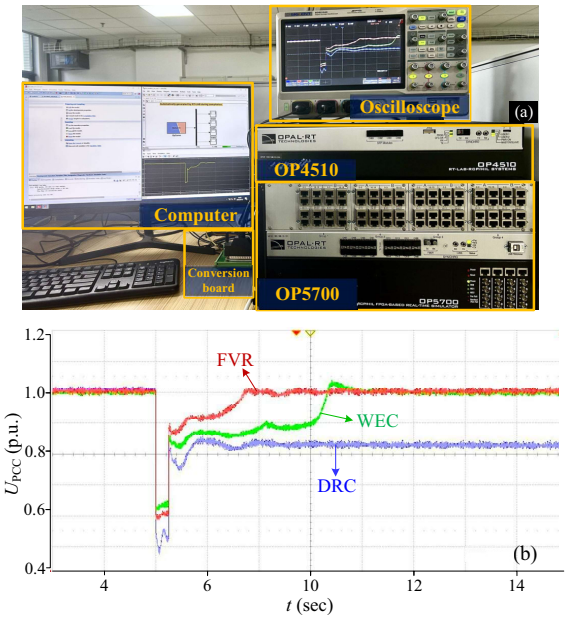

Fig. 18. Opal-RT real-time experimental platform and case results.(a) Experimental platform. (b)Voltage results of the case.

The system settings are from subsection IV-B. In particular, only the fault duration is set to 250ms to differentiate. From the results in Fig. 18(b), there is a significant drop in voltage after fault clearance with conventional DRC control. Moreover, the voltage remains at 0.82 p.u. after the voltage fluctuation. This is the voltage instability due to insufficient recovery support. For the WEC control, the voltage takes 3.27s to recover. As a comparison, the FVR control fast supports the voltage with a recovery time of 1.59s. Experimental results confirm the operational efficacy of FVR control in practical scenarios. Furthermore, this verifies the robustness, noise immunity, and adaptability of the control under non-ideal signal conditions.

V. Discussion

A. Discussion on Active Power and Reactive Power Contributions for Voltage Regulation

The validity and uniqueness of utilizing active power regulation as a voltage support method in this paper are discussed. It is a common view nowadays that reactive power is more capable of supporting voltage. However, this law is not fully consistent in weak grid and low voltage scenarios. Analogous to the analysis of active power in Section II, the contribution of reactive power increase to U_{PCC} is as follows.

$$\zeta_{Q-U} = \frac{\lambda}{2U_{\text{PCC}}\,\text{SCR}}\left[1+\frac{U_k^2\,\text{SCR}+2\alpha\lambda(P_{\text{WF}}-Q_{\text{WF}}\alpha)}{M_1}\right] \tag{15}$$

The condition where active power absorption contributes more to voltage than reactive power release is $-\zeta_{P-U} > \zeta_{Q-U}$. The derivation is:

$$\begin{aligned} &-[\text{SCR}\,U_k^2\alpha+\alpha M_1+2\lambda(-P_{\text{WF}}+Q_{\text{WF}}\alpha)] > \text{SCR}\,U_k^2 \\ &+2\alpha\lambda(P_{\text{WF}}-Q_{\text{WF}}\alpha)+M_1 \\ &\Leftrightarrow \text{SCR}\,U_k^2+M_1 < \frac{2\lambda(P_{\text{WF}}-Q_{\text{WF}}\alpha)(1-\alpha)}{1+\alpha} \end{aligned} \tag{16}$$

where the formula for M_1 is given in Eq. (7). in Section II.

A simplified equation for neglecting α is given.

$$\text{SCR}\,U_k^2+M_1 < 2\lambda P_{\text{WF}} \tag{17}$$

It is clear from Eq. (17) that the contribution of active power absorption is better under these characteristics: (a) the weaker the grid (lower SCR), (b) the larger the voltage drop (lower U_k), and (c) the longer the transmission line from the wind farm to the grid (larger λ).

The results of $-\zeta_{P-U}$ and ζ_{Q-U} with varying SCR are shown in Fig. 19. The results presented represent a representative case study under typical operating conditions. Table IV illustrates the parameters of the operating condition. In detail, A and B are the intersection points of $-\zeta_{P-U}$ and ζ_{Q-U} for the two typical cases, respectively. Conclusively, when the SCR is less than the critical value SCR_{lim1}, $-\zeta_{P-U}$ is greater than ζ_{Q-U}. Therefore, there is a tendency that the contribution to U_{PCC} by absorbing active power is better than reactive power in weak grids, as shown in the orange area of Fig. 19. This situation is different from that in the existing universal strong grid.

TABLE IV
Parameters for Voltage Regulation Comparison

Parameters	Value (p.u.)	Parameters	Value (p.u.)
λ	0.33	Q_{WF}	0.70
U_{PCC}	0.60	P_{WF1}	0.62
α	0 (approximation)	P_{WF2}	0.60

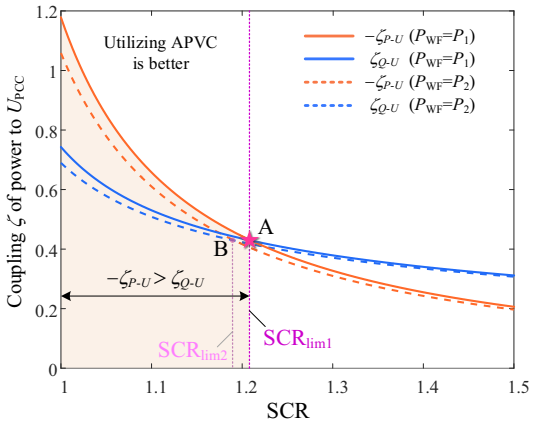

Fig. 19. Comparison of active power and reactive power contribution to voltage at different SCRs.

B. Analysis and Validation of APVC Simplification

There is a minor numerical difference between APVC with or without neglecting α. For $\alpha < 0.2$, the difference is negligible. This work specifically targets the scenario of wind farms connected to the grid via high-voltage transmission lines. In such a scenario, the X/R ratio is high, leading to α typically as 0.1 or lower in the practical systems [36], [37]. Thus, this simplification can be employed for analysis and calculation. The results of detailed APVC ($\alpha \neq 0$) in Eqs. (6)-(7) are as Fig. 20(a) for comparison with the simplified APVC in Eqs. (8)-(9). Additionally, a simulation verification of the simplified APVC under SCR = 1.2 is illustrated in Fig. 20(b). The settings are from subsection IV-B with DRC control to present the general time-series coupling. From Fig.20 and Fig.2, the difference between detailed APVC and simplified APVC is minor. This difference does not fundamentally impact the FVR control. The difference can be effectively mitigated by only a minor adjustment of the coupling threshold ζ_{low} of the stage switching module (adjustment gap is 0.03 in the example), as shown in the red curve in Fig.20(b). Notably, the characteristics of detailed APVC are identical to those of the simplified APVC analyzed in Section II. Therefore, the analysis of the APVC characteristics is confirmed to be correct. Besides, both the detailed and simplified APVC are applicable for FVR control. In practical monitoring applications, employing the simplified APVC eliminates the need to acquire the specific value of α, avoiding the need for R/X monitoring and the additional computational burden.

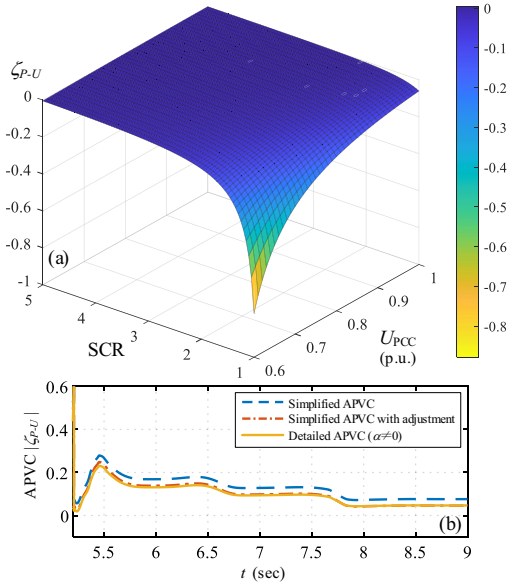

Fig. 20. Comparison of detailed and simplified APVC with $\alpha = 0.10$. (a) Detailed APVC with different SCR and U_{PCC}. (b) Simulation verification.

VI. Conclusion

This paper proposes a fast voltage recovery (FVR) control for the wind farm with ESS in weak grids, explicitly incorporating active power and voltage coupling (APVC). The characteristics of APVC are revealed by analysis. The active power increase has a negative effect on voltage recovery, which is more significant in weak grids and low-voltage scenarios. For the time-series properties, the coupling is strong in the early recovery stage and weak in the later recovery stage. Based on these insights, the FVR control is carefully designed. The core of the FVR control for supporting voltage is to transform the negative effect of APVC into a positive one. This transformation is achieved through ESS absorbing active power in the early recovery stage. Additionally, a Q-Logistic reactive power release method for WTGs further enhances voltage recovery performance. In the case studies of two different-scale IEEE systems and the real-time experimental platform, the proposed FVR control effectively supports voltage recovery in weak grids. Compared to existing methods, FVR control performs superiorly in terms of voltage dynamics, and short-term voltage stability. From various scenarios involving different dynamic load ratios and fault conditions, the voltage recovery time is reduced by 26.9% on average. This improvement is more than 40% in severe conditions. Moreover, this enhancement is maintained under the effect of the time latency. Across the diverse conditions, the adaptability and robustness of the proposed scheme are verified.

Appendix A
Simulation Model Parameters and Wake Effects

TABLE V
Parameters of the Simulation Model

	Parameters and description	Value
Parameters of WTGs	Radius of the WTG r_0	63 m
	Decay coefficient α	0.05
	Thrust coefficient $C_{T,i}$	0.588
	Distance between columns x_{ij}	600 m
	Distance between rows d_{ij}	600 m
	PI coefficients of the PLL $k_{\text{pp}}, k_{\text{ip}}$ (p.u.)	50, 6000
	Transformer ratio λ_{w}	0.69/35 kV
	DC voltage V_{dcw}	1.5 kV
	DC capacitance C_{dcw}	125 mF
Parameters of ESS	DC voltage V_{dces}	1 kV
	DC capacitance C_{ess}	0.5 mF
	Rated active power P_{Ness}	100 MW
	Rated energy capacity W_{batt}	200 MWh
Parameters of the integration system	Nominal AC frequency f_{N}	50 Hz
	Base capacity S_{B}	100 MVA
	AC system rated voltage V_{N}	220 kV
	AC line resistance r_{l}	0.0529 Ω/km
	AC line inductor x_{l}	0.529 Ω/km

The Jensen's model is used to describe the wake effect based on the above parameters [38].

$$V_j = V_0 \left[1 - \sum_{i=1}^{n} \left(1 - \sqrt{1 - C_{T,i}} \right) \cdot \xi_{ij} \right] \tag{18}$$

$$\xi_{ij} = \left(\frac{r_0}{r_i} \right)^2 \frac{A_s}{A_0} \tag{19}$$

$$r_i = r_0 + x_{ij} \cdot \tan\alpha \approx r_0 + x \cdot \alpha \tag{20}$$

where A_0 is the sweep area of WTG. The downstream WTG is partly shadowed by the upstream WTG. A_s is the shadowed area. Radius r_i describes the expansion effect of the wake.

References

[1] J. Xiao, P. Wang, S. Huang, Q. Luo, W. Chen, and J. Wei, "Virtuality-reality combination control for wind farm maximum power generation with wake model dynamic calibration," *IEEE Trans. Sustain. Energy*, vol. 16, no. 2, pp. 1007–1020, Apr. 2025.

[2] "Global wind report 2024," Global Wind Energy Council (GWEC), Brussels, Belgium, Tech. Rep., Apr. 2024, [Online]. Available: https://gwec. net/global-wind-report-2024/.

[3] X. Wang, J. Zhou, B. Qin, and L. Guo, "Coordinated power smoothing control strategy of multi-wind turbines and energy storage systems in wind farm based on MADRL," *IEEE Trans. Sustain. Energy*, vol. 15, no. 1, pp. 368–380, Jan. 2024.

[4] N. Verma, N. Kumar, and R. Kumar, "Battery energy storage-based system damping controller for alleviating sub-synchronous oscillations in a DFIG-based wind power plant," *Prot. Control Mod. Power Syst.*, vol. 8, no. 2, pp. 1–18, Apr. 2023.

[5] C. Li, S. Wang, F. Colas, and J. Liang, "Dominant instability mechanism of VSI connecting to a very weak grid," *IEEE Trans. Power Syst.*, vol. 37, no. 1, pp. 828–831, Sep. 2021.

[6] Z. Lv, B. Wang, Q. Guo, and H. Sun, "Optimal grid-support strategy with inverter-interfaced distributed generators for short-term voltage stability improvement," *IEEE Trans. Sustain. Energy*, vol. 15, no. 1, pp. 499–512, Jan. 2024.

[7] R. K. Varma and S. Mohan, "Mitigation of fault induced delayed voltage recovery (FIDVR) by PV-STATCOM," *IEEE Trans. Power Syst.*, vol. 35, no. 6, pp. 4251–4262, Nov. 2020.

[8] K. Kawabe and K. Tanaka, "Impact of dynamic behavior of photovoltaic power generation systems on short-term voltage stability," *IEEE Trans. Power Syst.*, vol. 30, no. 6, pp. 3416–3424, Nov. 2015.

[9] S. Asadollah, R. Zhu, and M. Liserre, "Analysis of voltage control strategies for wind farms," *IEEE Trans. Sustain. Energy*, vol. 11, no. 2, pp. 1002–1012, Apr. 2020.

[10] Q. Zong, W. Yao, H. Zhou, Y. Xiong, W. Gan, and J. Wen, "Hierarchical optimal frequency support scheme of wind farm with both grid-forming and grid-following wind turbines," *Int. J. Electr. Power Energy Syst.*, vol. 165, p. 110463, Apr. 2025.

[11] E. O. N. GmbH, "Grid code: High and extra high voltage," Tech. Rep., Jan. 2022, [Online]. Available: http:// www.eon.com/en/ energy-grids.html.

[12] H. Geng, L. Liu, and R. Li, "Synchronization and reactive current support of PMSG-based wind farm during severe grid fault," *IEEE Trans. Sustain. Energy*, vol. 9, no. 4, pp. 1596–1604, Oct. 2018.

[13] D.-Y. Gau and Y.-K. Wu, "Overview of reactive power and voltage control of offshore wind farms," in *Proc. 2020 Int. Symp. Comput., Consum. Control (IS3C)*, Nov. 2020, pp. 276–279.

[14] P. Mahish and S. Mishra, "Synchrophasor data based QV droop control of wind farm integrated power systems," *IEEE Trans. Power Syst.*, vol. 38, no. 1, pp. 358–370, Jan. 2023.

[15] Y. Guo and H. Gao, "Data-driven online system equivalent for self-adaptive droop voltage control of wind power plants," *IEEE Trans. Energy Convers.*, vol. 35, no. 1, pp. 302–305, Mar. 2020.

[16] J. Kim, J.-K. Seok, E. Muljadi, and Y. C. Kang, "Adaptive Q-V scheme for the voltage control of a DFIG-based wind power plant," *IEEE Trans. Power Electron.*, vol. 31, no. 5, pp. 3586–3599, May 2016.

[17] M. A. Mostafa and E. A. El-Hay, "An overview and case study of recent low voltage ride through methods for wind energy conversion system," *Renew. Sust. Energ. Rev.*, vol. 183, p. 113521, Sep. 2023.

[18] L. Li, C. Yang, H. Xu, Q. Yan, S. Zhou, and H. Yang, "Coordinated voltage control for offshore wind farm equipped with SVG and energy storage," in *Proc. 2022 12th Int. Conf. Power Energy Syst. (ICPES)*, Dec. 2022, pp. 800–804.

[19] J. Duan, B. Chen, J. Wang, and Y. Yue, "Adaptive control strategy for direct-drive wind turbine and energy storage to actively support grid voltage," in *Proc. 2023 4th Int. Conf. Power Eng. (ICPE)*, Dec. 2023, pp. 127–132.

[20] B. Li, D. Zheng, B. Li, X. Jiao, Q. Hong, and L. Ji, "Analysis of low voltage ride-through capability and optimal control strategy of doubly-fed wind farms under symmetrical fault," *Prot. Control Mod. Power Syst.*, vol. 8, no. 2, pp. 1–15, Apr. 2023.

[21] S. Zheng, D. Song, M. Su, X. Yang, Y. H. Joo *et al.*, "Comprehensive optimization for fatigue loads of wind turbines in complex-terrain wind farms," *IEEE Trans. Sustain. Energy*, vol. 12, no. 2, pp. 909–919, Apr. 2021.

[22] L. Xue, T. Niu, S. Fang, and Z. Li, "Parameter optimization for VAR planning of systems with high penetration of wind power: An adaptive equivalent reduction method," *IEEE Trans. Sustain. Energy*, vol. 14, no. 4, pp. 1950–1963, Oct. 2023.

[23] J. Ouyang, T. Tang, J. Yao, and M. Li, "Active voltage control for DFIG-based wind farm integrated power system by coordinating active and reactive powers under wind speed variations," *IEEE Trans. Energy Convers.*, vol. 34, no. 3, pp. 1504–1511, Sep. 2019.

[24] M. Li, X. Zhang, Z. Guo, H. Pan, M. Ma, and W. Zhao, "Impedance adaptive dual-mode control of grid-connected inverters with large fluctuation of SCR and its stability analysis based on D-partition method," *IEEE Trans. Power Electron.*, vol. 36, no. 12, pp. 14 420–14 435, Dec. 2021.

[25] L. Asiminoaei, R. Teodorescu, F. Blaabjerg, and U. Borup, "A digital controlled PV-inverter with grid impedance estimation for ENS detection," *IEEE Trans. Power Electron.*, vol. 20, no. 6, pp. 1480–1490, Nov. 2005.

[26] G. Lammert, D. Premm, L. D. P. Ospina, J. C. Boemer, M. Braun, and T. Van Cutsem, "Control of photovoltaic systems for enhanced short-term voltage stability and recovery," *IEEE Trans. Energy Convers.*, vol. 34, no. 1, pp. 243–254, Mar. 2019.

[27] Y. Lan, S. Wei, W. Yao, Y. Zhang, Y. Yang, and J. Wen, "Reapplication of training set: A physically reliable framework for power systems dominant instability mode identification using similar samples," *IEEE Trans. Power Syst.*, 2025, Early Access.

[28] X. Yuan, Z. Du, Y. Li, Y. Xu, J. Li, D. Yu, H. Peng, and Z. Xu, "Two-stage coordinated control of type-4 wind turbine with grid-forming ability for active damping support," *IEEE Trans. Energy Convers.*, vol. 39, no. 2, pp. 817–830, Jun. 2024.

[29] P. S. Kundur and O. P. Malik, *Power system stability and control*. McGraw-Hill Education, 2022.

[30] C. Wang, Z. Wang, J. Wang, and D. Zhao, "Robust time-varying parameter identification for composite load modeling," *IEEE Trans. Smart Grid*, vol. 10, no. 1, pp. 967–979, Jan. 2019.

[31] *IEC 61400-25: Wind Turbines - Part 25: Communications for Monitoring and Control of Wind Power Plants*, International Electrotechnical Commission Standard, 2021.

[32] M. Wei and Z. Chen, "Study of LANs access technologies in wind power system," in *IEEE PES Gen. Meet.*, Jul. 2010, pp. 1–6.

[33] M. A. Ahmed, W.-H. Yang, and Y.-C. Kim, "OPNET simulation model for small scale wind power farm monitoring based on IEC 61400-25," in *2012 Asia-Pac. Power Energy Eng. Conf.*, Mar. 2012, pp. 1–5.

[34] M. Shadaei, J. Khazaei, and F. Moazeni, "Data-driven nonlinear model predictive control for power sharing of inverter-based resources," *IEEE Trans. Energy Convers.*, vol. 39, no. 3, pp. 2018–2031, Sep. 2024.

[35] Y. Mi, J. Guo, Y. Fu, C. Wang, and P. Wang, "Accurate power allocation of multienergy storage island DC microgrid based on virtual power rating," *IEEE Trans. Power Electron.*, vol. 38, no. 1, pp. 261–270, Jan. 2023.

[36] L. Xiong, X. Liu, L. Liu, and Y. Liu, "Amplitude-phase detection for power converters tied to unbalanced grids with large X/R ratios," *IEEE Trans. Power Electron.*, vol. 37, no. 2, pp. 2100–2112, Feb. 2022.

[37] S.-C. Moon, H.-S. Park, and K.-J. Kim, "Effects review on transformer and line impedance by X/R ratio in power system," in *IEEE 2013 Tencon-Spring*, Apr. 2013, pp. 68–70.

[38] S. Ma, H. Geng, G. Yang, and B. C. Pal, "Clustering-based coordinated control of large-scale wind farm for power system frequency support," *IEEE Trans. Sustain. Energy*, vol. 9, no. 4, pp. 1555–1564, Oct. 2018.

Qihang Zong received the B.S. degree in electrical engineering from Hefei University of Technology, Hefei, China, in 2021. From 2024 to 2025, he was a visiting Ph.D. student at the Cardiff University, Wales UK. He is currently working toward the Ph.D. degree in electrical engineering at Huazhong University of Science and Technology (HUST), Wuhan, China. His research interests include frequency and voltage stability analysis and control of power systems with renewable energy.

Wei Yao (Senior Member, IEEE) received the B.S. and Ph.D. degrees in electrical engineering from Huazhong University of Science and Technology (HUST), Wuhan, China, in 2004 and 2010, respectively.

He was a Post-Doctoral Researcher with the Department of Power Engineering, HUST, from 2010 to 2012 and a Postdoctoral Research Associate with the Department of Electrical Engineering and Electronics, University of Liverpool, Liverpool, U.K., from 2012 to 2014. Currently, he has been a Professor with the School of Electrical and Electronics Engineering, HUST, Wuhan, China. His current research interests include power system stability analysis and control, renewable energy, HVDC and DC Grid, and application of artificial intelligence in Smart Grid.

Hongyu Zhou received the B.S. degree in electrical engineering from Southwest Jiaotong University (SWJTU), Chengdu China in 2020, and the Ph.D. degree in electrical engineering from the Huazhong University of Science and Technology, Wuhan China in 2025. His current research interests include stability analysis and control of power system with bulk renewable energy, and AC/DC hybrid power system.

Jun Liang (Fellow, IEEE) received the BSc degree from Huazhong University of Science and Technology, Wuhan China in 1992, and the MSc and PhD degrees from China Electric Power Research Institute, Beijing China in 1995 and 1998 respectively. From 1998 to 2001, he was a Senior Engineer with China Electric Power Research Institute. From 2001 to 2005, he was a Research Associate at Imperial College London, UK. From 2005 to 2007, he was a Senior Lecturer at the University of Glamorgan, Wales UK. Currently, he is a Professor at the School of Engineering, Cardiff University, Wales UK. His research interests include DC transmission and distribution, power electronics converter control, power system stability, and renewable power generation.

Yongxin Xiong (Member, IEEE) received the B.S. and Ph.D. degrees in electrical engineering from the Huazhong University of Science and Technology, Wuhan, China, in 2017 and 2022, respectively. He was a Postdoctoral Researcher with Energy Department, Aalborg University, Aalborg, Denmark, from 2022 to 2024. He is currently a Postdoctoral Researcher with the Department of Electrical and Electronic Engineering, Hong Kong Polytechnic University, Hong Kong, China. His research interests include power system stability analysis and control, renewable energy, HVDC and DC Grid, and the coordination of control and system protections in grid-following and grid-forming VSC-connected systems.

Jinyu Wen (Senior Member, IEEE) received the B.S. and Ph.D. degrees in electrical engineering from Huazhong University of Science and Technology (HUST), Wuhan, China, in 1992 and 1998, respectively.

He was a visiting student from 1996 to 1997 and Research Fellow from 2002 to 2003 all at the University of Liverpool, Liverpool, UK, and a Senior Visiting Researcher at the University of Texas at Arlington, Arlington, USA, in 2010. From 1998 to 2002 he was a Director Engineer with XJ Electric Co. Ltd. in China. In 2003, he joined the HUST and now is a Professor with the School of Electrical and Electronics Engineering, HUST. His current research interests include renewable energy integration, energy storage, multi-terminal HVDC and power system operation and control.